Nonlinear density scaling of spin noise reveals atomic correlations in warm vapors

J. Delpy,[1,2,*] E. Cardoz,[1] K. V. Adwaith,[1] N. Fayard,[1] N. Belabas,[3] F. Bretenaker,[1] and F. Goldfarb[1]

[1] *Université Paris-Saclay, CNRS, École Normale Supérieure Paris-Saclay, CentraleSupélec, LuMIn, Orsay, France*

[2] *Department of Applied Physics, University of Geneva, 1205 Geneva, Switzerland*

[3] *Centre de Nanosciences et de Nanotechnologies, CNRS, Université Paris-Saclay, 91120 Palaiseau, France*

(Received 29 May 2026; accepted 14 July 2026; published 8 September 2026)

We experimentally demonstrate a nonlinear dependence of the spin-noise variance on atomic density in a warm alkali vapor. Implementing high-bandwidth spin-noise spectroscopy (SNS) near the D_2 transition of rubidium, a quadratic spin-noise contribution is shown to arise at high densities, in contrast with the linear dependence valid in noninteracting ensembles. This nonlinear scaling is shown to crucially depend on the residual optical excitation of the vapor by the probe beam, suggesting it stems from atomic cross correlations due to resonant dipole-dipole interaction (ddi) in the vapor. We support this claim by introducing an additional experimental protocol to quench the ddi, resulting in a suppression of both the quadratic scaling of the spin variance and the distortions of the spin-noise spectrum induced by the interaction. These results extend the applications of SNS to the characterization of many-body correlations in complex quantum systems.

DOI: 10.1103/dy7y-qllc

I. INTRODUCTION

Spin properties lie at the heart of numerous quantum technologies, from metrology sensors to electronic devices. Some of them, such as optically pumped magnetometers (OPM) [1,2], atomic clocks [3,4], or quantum storage platforms [5–7], rely on the manipulation of noninteracting spin ensembles. In contrast, the second quantum revolution is led by technologies exploiting nonclassical correlations between particles [8], such as quantum communication and cryptography [9,10].

A powerful experimental method to probe spin dynamics in a wide variety of systems is the so-called spin-noise spectroscopy (SNS) [11]. Optically measuring spontaneous fluctuations of the total spin in an ensemble allows to characterize its structural and coherence properties. SNS was successfully performed in noninteracting systems such as atomic vapors [12–15], bulk and low-dimensional semiconductors [16–19], and solid-state spins [20,21]. This method reveals both the fundamental mechanisms and the limitations in such systems by identifying noise and decoherence channels, even far from equilibrium [22–26]. This proves useful when engineering, for instance, quantum sensors such as OPM, in which spin noise (SN) often limits sensitivity [27–29], promoting the use of atomic and light squeezed states [30–32].

Nevertheless, implementations of SNS in correlated systems are scarce. Spin fluctuations detected by optical interferometry revealed entanglement in an ultracold Fermi gas a decade ago [33], yet the current SNS protocol could only detect artificially driven spin noise in cold atoms [34]. In alkali vapors, a frequency redistribution across spin-noise spectra was shown to originate from spin-exchange collisions [35–37], although no signatures of atomic correlations were found in the total spin-noise variance. The technical challenge of implementing SNS in more complex systems persists to this day, despite several theoretical proposals suggesting that SNS could be used to probe spin interactions [38], magnetic phase transitions [39], or many-body localization [40].

To contribute bridging the gap between noninteracting and strongly correlated ensemble, we study SNS in a warm rubidium vapor. We reported in Ref. [41] distortions of spin-noise spectra originating from dipole-dipole interactions arising between atoms in a ground state and a residual excited-state population excited by the probe light. These previous observations clearly indicated the breakdown of the single-atom description, but the narrow detection bandwidth prevented an unambiguous observation of many-body correlations. In the present work, we aim at providing a clear proof of such correlations by measuring the density scaling of the absolute spin-noise variance, whose deviation from linearity directly reflects correlated spin fluctuations.

This paper is organized as follows: Section II introduces the experimental setup used to perform SNS measurements with a high bandwidth over two orders of magnitude of the vapor density. We report a quadratic scaling of the spin-noise variance with density occurring at high temperatures. In Sec. III, we analyze the dependence of this anomalous scaling on the residual optical vapor excitation by investigating the impact of the probe laser parameters. This leads us to interpret our observations in terms of correlated atomic spin noise induced by optical interactions. Finally, Sec. IV supports this interpretation by introducing a novel optical method to quench

*Contact author: joseph.delpy@unige.ch

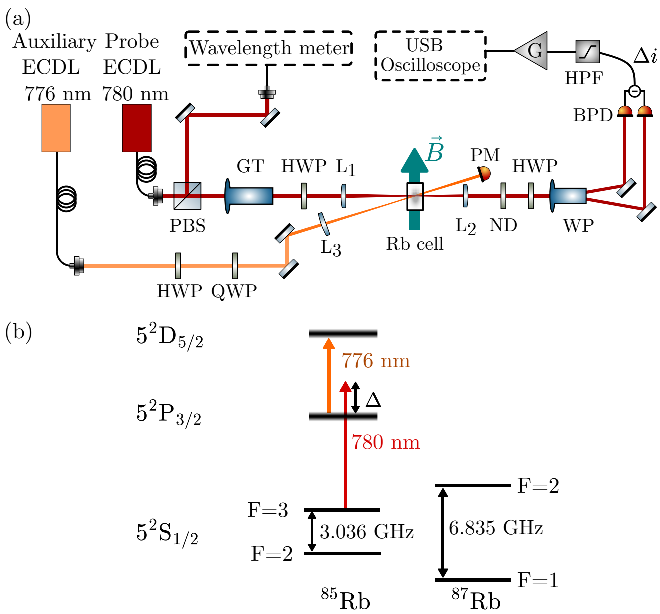

FIG. 1. Experimental setup and energy structure of rubidium. (a) Schematics of the experimental setup. The 780 nm probe beam is linearly polarized using a Glan-Thompson (GT) polarizer before entering the 1 mm rubidium vapor cell. Output polarization fluctuations are measured using a balanced detection scheme comprising a half-wave plate (HWP), a Wollaston prism (WP), and a balanced photodiode (BPD). The detected power is adjusted using a variable neutral density filter (ND). A magnetic field $\vec{B}$ is applied transversely. The role of the auxiliary 776 nm laser (depicted in orange) is discussed in Sec. IV. L_1, L_2, L_3: focusing and collimation lenses, QWP: quarter-wave plate, PBS: polarizing beamsplitter, and PM: powermeter. A bias tee acts as a high-pass filter (HPF) and G denotes a low-noise amplifier. (b) Diagram of energy levels involved in this study. F numbers denote ground-state hyperfine levels. The laser detuning Δ is defined in the main text.

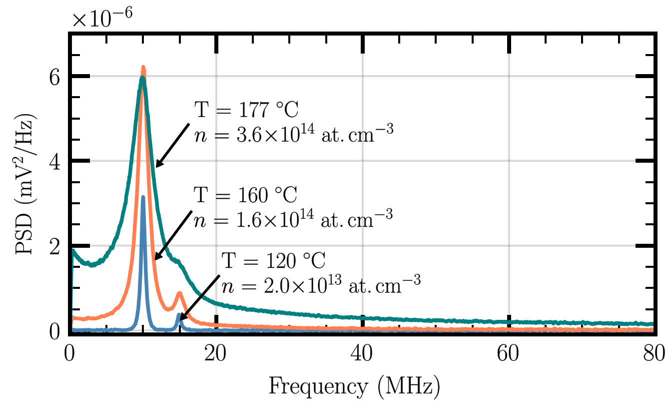

FIG. 2. Experimental spin-noise spectra. Examples of spin noise PSD obtained for densities below and above 10^{14} at. cm^{-3}, for a detuning $\Delta/2\pi = +1.5$ GHz and a 2 mW input probe power.

dipole-dipole interactions and measure subsequent changes in the spin-noise variance.

II. EXPERIMENTAL MEASUREMENT OF NONLINEAR SPIN-NOISE VARIANCE

A. Experimental setup and method

A schematic of the experimental setup is shown in Fig. 1(a). We measure Faraday rotation fluctuations due to SN in a rubidium vapor by tuning an external cavity diode laser (ECDL, Toptica DL pro) near the D_2 line of rubidium atoms. A Glan-Thompson polarizer produces a high-purity linear polarization of the probe light, which is then focused to a diameter of $\phi \simeq 300$ µm inside the vapor cell. The latter consists of a 1-mm-thick glass cell filled with natural rubidium, without any buffer gas or antirelaxation coating. The cell is embedded in a metallic oven and heated using two 15 W resistors. Two T-type thermocouples measure the temperature in the vicinity of both the probed area and the Rb reservoir, with a $\pm 2\,^{\circ}$C estimated precision. The first temperature T is used to infer the vapor density using the Killian formula [42]. A home-made temperature controller acts as a switch to a dc power supply feeding current to the heating resistors. A magnetic field of 19 G corresponding to a Larmor frequency of $\simeq$10 MHz for ^{85}Rb and $\simeq$15 MHz for ^{87}Rb is applied in a Voigt configuration. This field shifts the spin-noise resonance from zero frequency to the corresponding Larmor frequencies of the two isotopes, above any dominating low-frequency technical noise [12]. Other noises, including the detection chain background and laser shot noise, are appropriately subtracted as elaborated in Appendix A. The cell along with the oven is shielded from any ambient magnetic field using a three-layer μ-metal shield.

This experimental setup allows to address densities spanning over 2 orders of magnitude. Even at the far detunings considered here, which are typically more than 5 times larger than the Doppler broadening of 250–320 MHz half width at half maximum (HWHM) in our experimental conditions, the absorption of the probe light becomes non-negligible at high density. To eliminate the dependence of the measured signal strength on the optical power incident on the photodetector, which varies with density because of absorption, we use a variable neutral density filter placed after the cell to keep the optical power reaching the detection stage constant. In the following, we refer to it as the "detected power," denoted by P_d, to distinguish it from the input probe power P_p in the cell. A Wollaston prism then splits the beam of power P_d into its orthogonal polarization components that are balanced using a half-wave plate. The balanced beams are sent to a 350 MHz bandwidth balanced photodetector (Thorlabs PDB435A) that produces a signal equal to the difference between the photocurrents corresponding to the two beams, $\Delta i \propto i_+ - i_-$. This differential current is, in turn, proportional to the instantaneous fluctuations in the rotation angle of the probe, $\Delta i \propto \delta\theta(t)$, and therefore to the instantaneous spin fluctuations [11]. A bias-tee filters out frequency components below 200 kHz, while the ac component is amplified with a 23.8 dB gain. This signal is fed into a USB oscilloscope (Pico Technology PicoScope 3418E MSO), with a 350 MHz analog bandwidth and a 1 GHz sampling rate, to digitize the data and compute the spin-noise power spectral density (PSD). Finally, the spin-noise variance is computed by integrating under the PSD [14]. The integration procedure is discussed in Appendix A.

Figure 2 shows typical spin-noise spectra at different atomic number densities obtained for a detuning

$\Delta/2\pi = +1.5$ GHz and an input probe power P_p of 2.0 mW. Here, the detuning is defined as $\Delta = \omega_p - \omega_0$, with ω_p the probe laser frequency and ω_0 the $5^2S_{1/2}$, $F = 3 \rightarrow 5^2P_{3/2}$ transition frequency of ^{85}Rb. The signal is detected at a fixed power $P_d = 400\,\mu$W for all densities. The noise spectrum corresponding to $n \simeq 2 \times 10^{12}$ at. cm^{-3} displays a standard spin-noise resonance peaking at the respective Larmor frequencies of ^{85}Rb and ^{87}Rb. The main noise and broadening source at such low atomic density is the finite transit time of atoms through the probe beam. However, for densities exceeding 10^{14} at. cm^{-3}, a clear additional broadening of the resonance peaks is observed, accompanied by a broadband noise component that lifts the baseline dramatically, especially at lower frequencies. This is prominently seen at $n \simeq 3.6 \times 10^{14}$ at. cm^{-3}. This long-tail component contributes to the total noise power up to frequencies as high as 200 MHz. These high-density effects have previously been attributed to resonant dipole-dipole interaction in the vapor when the average interatomic separation is less than the probe light's wavelength, i.e., $\langle r \rangle \lesssim \lambda/2\pi$ [41]. In the following, we study the effects of this interaction on the total spin-noise variance, which carries information on the interplay between the stochastic evolution of each atom [36].

B. Nonlinear density dependence of the absolute spin-noise variance

Figure 3(a) shows results of total spin-noise variance integrated from power spectra similar to the ones in Fig. 2, as a function of the vapor density, ranging from $n = 1.5 \times 10^{12}$ to 3.9×10^{14} at. cm^{-3} ($T = 80\,^\circ$C to $T = 179\,^\circ$C). The detuning is $\Delta/2\pi = +1.5$ GHz, corresponding to a probe laser tuned between the $F = 3 \rightarrow F'$ and $F = 2 \rightarrow F'$ transitions of rubidium 85. The input probe power is $P_p = 2$ mW, while the detected power is fixed at $P_d = 400\,\mu$W for all densities. The data show two distinct regimes in the evolution of the spin noise, below and above a characteristic density $n_c \simeq 1.5 \times 10^{14}$ at. cm^{-3}. For $n < n_c$, the spin-noise variance follows a linear trend up to densities on the order of 10^{14} at. cm^{-3}, as expected for noninteracting vapors [12,14]. In this regime, a simple linear regression (in red dashed line) yields a slope of $\kappa_{\rm exp} = 0.138 \pm 0.02\,{\rm nV}^2\,{\rm cm}^3$. Error bars on the spin-noise variance are due to uncertainties in the background subtraction (see Appendix A), while errors on the density arise from uncertainties in the temperature inside the cell. To validate our spin-noise and density measurements, we compare this value with a light-atom coupling model [27,43], accounting for the hyperfine structure of rubidium and our experimental parameters. Assuming uncorrelated atoms, we obtain a theoretical slope $\kappa_{\rm th} = 0.130\,{\rm nV}^2\,{\rm cm}^3$, in good agreement with the experimental slope $\kappa_{\rm exp}$. The complete calculations can be found in Appendix C. This confirms that the spin noise is consistent with that of independent rubidium atoms close to thermal equilibrium.

Strikingly, a strong deviation from this linear regime is then observed for densities $n > n_c$. The SN power visibly increases faster than expected, reaching absolute values around 40% higher at $n = 3.9 \times 10^{14}$ at. cm^{-3} than predicted by the previous linear scaling. This superlinear increase is further evidenced in Fig. 3(b), which shows the residuals from the

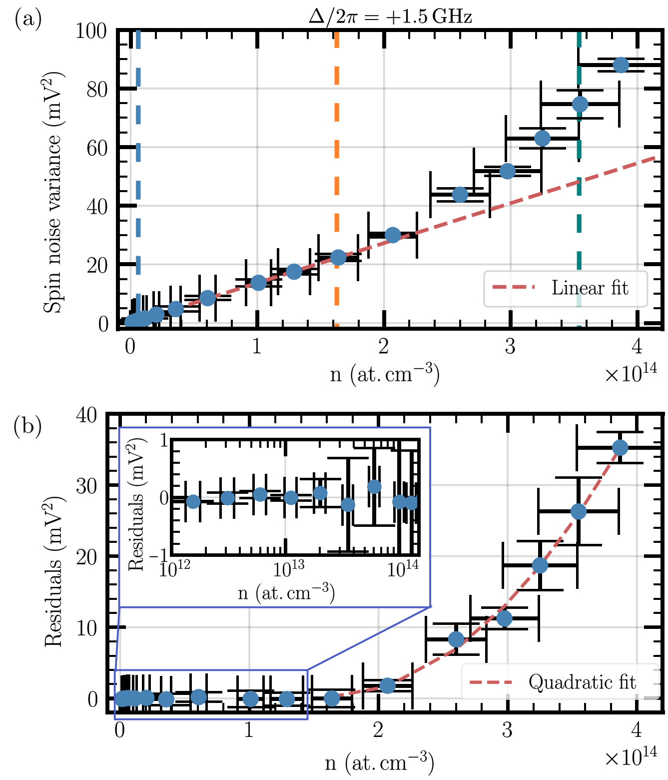

FIG. 3. Evolution of the absolute spin-noise variance with vapor density. (a) Evolution of the integrated spin-noise variance as a function of atom density for a detuning $\Delta/2\pi = +1.5$ GHz, a 2 mW probe power, and 0.4 mW detected power. Red dashed line: linear fit to the data up to $n = 10^{14}$ at. cm^{-3}. Color dashed lines indicate the corresponding spin noise PSD in Fig. 2. (b) Residuals from the linear regression, fitted with a quadratic function for $n > 1.5 \times 10^{14}$ at. cm^{-3} (red dashed line). Inset: Close-up view of the low-density data points.

linear fit at low densities. The fact that this deviation appears at a threshold rather than continuously is demonstrated by the inset figure, which shows that all data points agree with the linear regression within measurement uncertainties below n_c. The residuals at higher densities can then well be fitted by a quadratic function with a density offset $f(n, n_c) = \gamma_{\rm exp}(n - n_c)^2$ (red dashed line), which is incompatible with the independent atom picture.

We note that a quadratic scaling of the Faraday rotation variance has been observed in cold atomic clouds and Bose-Einstein condensates [44–46], but was attributed to an undesired light backaction noise. Such a detrimental effect results from elliptical fluctuations of the probe beam polarization coupling to a residual spin magnetization via tensorial light shifts. In our experiment, however, due to the unresolved excited-state hyperfine structure, the tensorial polarizability of the vapor is negligible for large detunings [47,48]. Moreover, the vapor being unpolarized, we can discard nonlinearities due to probe backaction in our work. Finally, the quadratic spin noise cannot be imputed to the detection, since the detected power P_d is weak enough for the photodiodes to operate in a linear regime, as demonstrated in Appendix B.

Finally, the nonlinear spin-noise contribution seems to arise jointly with the distortions of the spin-noise spectra

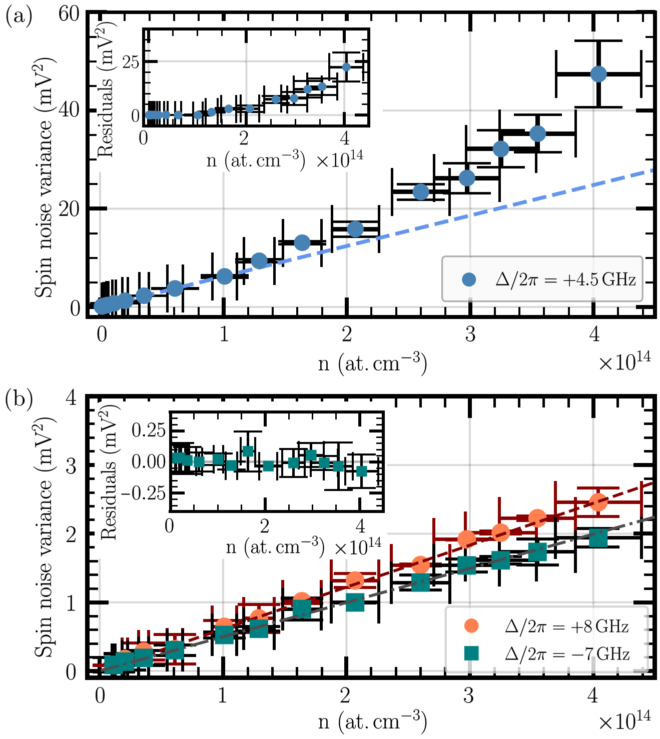

FIG. 4. Dependence of the spin-noise scaling on the probe detuning. Evolution of the spin-noise variance as a function of vapor density for a detuning of (a) $\Delta/2\pi = +4.5$ GHz and (b) $\Delta/2\pi = -7$ GHz (green squares), and $\Delta/2\pi = 8$ GHz (orange dots). Dashed and dash-dotted lines are linear fit to the data for $n < 10^{14}$ at. cm^{-3}. Insets: Residuals from linear fits from respective color-coded data.

discussed in Sec. II A and Ref. [41]. Such changes were attributed to resonant dipole-dipole interactions induced by the off-resonant probe beam. We therefore suggest that the superlinear spin-noise variance evidenced here could have the same origin. Specifically, it could arise from positive correlations between optically interacting atoms at high density. In the next section, we support this claim by investigating the dependence of the nonlinear spin variance on the residual excitation of the vapor by the probe beam.

III. CHARACTERIZATION OF OPTICALLY DRIVEN ATOM-ATOM SPIN-NOISE CORRELATIONS

Resonant dipole-dipole interactions describe the coherent energy exchange between atoms lying in a ground state and the small excited-state population induced by the detuned probe laser. This fraction is governed by the saturation parameter $s \propto \frac{\Omega^2}{\Delta^2+\Gamma_0^2/4}$ [49], where $1/\Gamma_0$ is the excited-state lifetime and Ω the probe Rabi frequency. Therefore, we expect a dependence of the observed nonlinear spin noise on the two parameters Ω and Δ, which we now experimentally investigate.

A. Impact of the optical detuning

We first evidence the impact of the probe light on atom-atom interactions by performing the previous measurement at different probe laser frequencies. Figure 4(a) shows the evolution of the spin-noise variance for a detuning $\Delta/2\pi = +4.5$ GHz, i.e., a probe laser tuned between the $F = 2 \rightarrow F'$ transitions of rubidium 85 and $F = 1 \rightarrow F'$ of rubidium 87 [see Fig. 1(b)]. The input and detected optical powers are the same as in the previous section. The results are similar to the ones described at $\Delta/2\pi = +1.5$ GHz. The spin noise can at first well be fitted up to $n = 10^{14}$ at. cm^{-3} with a simple linear regression (blue dashed line), while a strong deviation from the linear fit is observed at higher density.

Interestingly, such a nonlinear behavior is not observed for another set of larger detunings $\Delta/2\pi = -7$ GHz and $\Delta/2\pi = +8$ GHz, as shown in Fig. 4(b) in green squares and orange dots, respectively. These values correspond to a probe beam being respectively far red and blue detuned from all hyperfine transitions of both rubidium 85 and 87. In this case, a linear fit to the spin-noise variance for densities lower than or equal to $n = 10^{14}$ at. cm^{-3} (shown in green dash-dotted line and red dashed line, respectively) correctly predicts the spin-noise variance even at higher density. This is emphasized in the inset of Fig. 4(b), where residuals from the linear fit for the $\Delta/2\pi = -7$ GHz data are all zero within measurement errors. Note that the measured slope is much weaker than in Figs. 3(a) and 4(a) due to the larger detuning to all atomic hyperfine transitions. This linearity over more than 2 orders of magnitude for a far-detuned probe beam confirms the role of a light-induced excitation in the anomalous scaling shown in the previous sections.

B. Impact of the optical probe power

We now investigate the role of the input probe power, which we expect to enhance light-driven dipole-dipole interactions. Let us remind here that we keep the detected power constant throughout the measurements in a same set of data, by rotating a tunable neutral density filter placed after the cell. As a result, the integrated noise variance is not expected to depend on the input optical probe power.

This assumption has been tested by measuring the spin-noise variance for a fixed detuning $\Delta/2\pi = +1.5$ GHz as a function of an input probe power ranging from 1 to 3.5 mW, at different atomic densities. As compared to the previous sections, the detected power P_d has to be lowered to 160 μW due to the weak transmitted power for $P_p = 1$ mW at high density. Results are shown in Fig. 5. For the lowest density $n = 3.6 \times 10^{13}$ at. cm^{-3} (blue dots), the noise variance indeed remains constant whatever the input probe power, as expected. However, for a higher density value of 1.6×10^{14} at. cm^{-3} (orange squares), a net increase in the detected signal is visible. This is even more pronounced as the density reaches 2.6×10^{14} at. cm^{-3} (green triangles) and 3.3×10^{14} at. cm^{-3} (red diamonds). This shows that the quadratic spin-noise contribution present at high densities increases with the probe laser power, even though the amount of light reaching the detector is kept constant. This observation is in strong disagreement with the expected constant behavior for independent atoms, and confirms that the quadratic spin noise is indeed due to light-induced interactions at high density.

C. Interpretation based on a simple model of spin correlations

We now discuss our experimental results. First, we note that since we probe spin noise indirectly via Faraday

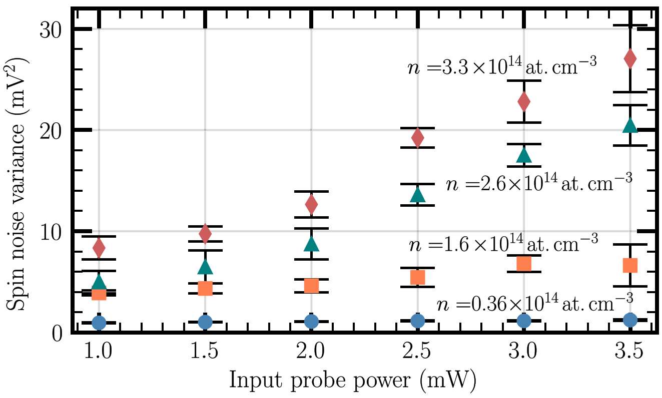

FIG. 5. Evolution of the measured spin-noise on the input probe power. Detected spin-noise variance as a function of input probe power for different vapor densities. The detected power is fixed to 160 μW for all points, and the detuning is $\Delta/2\pi = +1.5$ GHz.

rotation fluctuations, our observations could in principle stem from the complex optical response of the vapor at high density rather than the spin dynamics itself. Although the vapor density is a convenient experimental parameter to investigate atom-atom interactions in hot vapors, the optical depth experienced by the detuned probe at the highest densities reaches one. In this regime, multiple light scattering is no longer negligible but remains weak. In the following discussion, we choose to neglect the potential impact of photons detected after more than one scattering event on the Faraday rotation signal, as well as possible collective atomic dynamics induced by direct exchange of photons. On the other hand, spontaneously emitted photons escaping the cell are not phase related to the transmitted beam, so that their contribution to the balanced homodyne signal can be safely discarded.

Therefore, we attribute the nonlinear spin-noise signal to correlations between atoms at high density. Indeed, for a probe laser beam propagating along an arbitrary z direction, the Faraday rotation angle at the cell output is

$$\varphi = g \sum_{i=1}^{N} \left\langle s_z^{(i)} \right\rangle, \tag{1}$$

where the sum runs over the N probed atoms and $\langle s_z^{(i)} \rangle$ is the quantum average z component of the single-atom electronic spin operator. Here, $g = \frac{d_0^2 k}{6\epsilon_0 \hbar \Delta \Sigma}$, with Σ the probe beam area, is an optical coupling factor originating from the atomic polarizability (see Appendix C), which we implicitly assume constant for all atoms across the cell length and laser area. In this section, we overlook the nuclear spin degree of freedom and the resulting hyperfine structure to simplify the discussion. In a nonmagnetized ensemble of atoms experiencing independent stochastic trajectories, spin noises incoherently add up, so that the variance of the Faraday rotation angle is

$$\langle \varphi^2 \rangle = g^2 \sum_{i=1}^{N} \left\langle \left(s_z^{(i)}\right)^2 \right\rangle \propto n \left\langle s_z^2 \right\rangle, \tag{2}$$

where $\langle s_z^2 \rangle$ denotes the single-particle variance of all atoms in an identical thermal state. For a small perturbation induced by the probe beam, as in our experiment, one can assume the ensemble close to thermal equilibrium. The variance $\langle s_z^2 \rangle$ is then solely determined by the ground-state properties and the vapor temperature [35]: $\langle s_z^2 \rangle = \mathrm{Tr}(\rho_{\mathrm{th}}^{(1)} s_z^2)$, where $\rho_{\mathrm{th}}^{(1)}$ is the single-body thermal state density matrix. Since $\langle s_z^2 \rangle$ is independent of the density, according to Eq. (2) the resulting detected spin noise is linear with n, in agreement with our experimental results at low vapor densities.

At higher density, if atomic interactions are strong enough to induce correlations between individual spin dynamics, Eq. (2) has to be modified to take into account pairwise cross correlations

$$\langle \varphi^2 \rangle = g^2 \left[\sum_{i=1}^{N} \left\langle \left(s_z^{(i)}\right)^2 \right\rangle + \sum_{i}^{N} \sum_{j \neq i}^{N} \frac{\left\langle s_z^{(i)} s_z^{(j)} + s_z^{(j)} s_z^{(i)} \right\rangle}{2} \right]. \tag{3}$$

Although the amplitude of the two-body correlations certainly depends on n, owing to the Cauchy-Schwartz inequality, it admits the constant single-particle variance as an upper bound: $\langle s_z^{(i)} s_z^{(j)} + s_z^{(j)} s_z^{(i)} \rangle \leqslant \langle 2(s_z^{(i)})^2 \rangle$. The second term in Eq. (3) is thus expected to maximally grow as the squared atomic density n^2. At sufficiently high densities, the signal is thus expected to follow

$$\langle V^2 \rangle \propto g^2(\beta n + \gamma n^2), \tag{4}$$

where β describes the *uncorrelated* part of the noise and is related to the equilibrium state of the vapor, and γ parametrizes the *correlated* fraction of the noise. This simple model matches our experimental observation of an additional nonlinear density contribution to the spin-noise variance. Moreover, our results suggest that the cross-correlation coefficient γ depends on the vapor optical excitation via the light Rabi frequency Ω and detuning Δ to nearby atomic transitions: $\gamma = f(\Omega, \Delta)$.

Nevertheless, the fact that the nonlinear spin-noise scaling is only observed for densities higher than $n_c \simeq 10^{14}$ at. cm^{-3} is not inherently captured by the simple model described above. As noted in Sec. II B, the spin-noise variance cannot be fitted by a single equation such as Eq. (4) across the whole density range. Instead, we resort to the discontinuous model described above, where we first use a linear regression with a slope κ_{exp} before adding a quadratic contribution $\propto (n - n_c)^2$ at higher densities. Given our current experimental precision, whether this density threshold effect results from a genuine nonanalytical behavior rather than a sharp density dependence of the correlation coefficient γ cannot be definitively settled.

In both cases, our experimental results emphasize that the high-density spin noise is intrinsically many body, with *positive* correlations between atoms in this case. Reproducing these results requires a many-body noise model beyond the widely used mean-field Bloch equations [35] and the two-body model introduced in Ref. [41]. Moreover, deeper analysis of the latter revealed an important discrepancy between the amplitude of the measured and predicted low-frequency broadband noise (described in Sec. II B), which also suggests the limit of the two-atom picture. Going beyond this framework to describe correlations requires to explicitly model the dynamics of a many-body ensemble interacting with light, a theoretical challenge we let for future work.

In order to bring additional experimental evidence to this discussion, the next section introduces a protocol aiming at tuning the strength of the dipole-dipole interactions. In contrast with the previous sections, we thus investigate changes in the nonlinear spin noise contribution at a constant atomic density, while the excited-state population is quenched by a second laser.

IV. SUPPRESSION OF CORRELATIONS USING AN AUXILIARY RESONANT BEAM

A. Excitation scheme and protocol

Suppression of resonant dipole-dipole interactions is achieved by depopulating the $5^2P_{3/2}$ excited state through the 776 nm $5^2P_{3/2} \rightarrow 5^2D_{5/2}$ transition. The relevant energy levels scheme is shown in Fig. 1(b). We use a second Toptica ECDL for the auxiliary beam, distinct from the probe beam. This auxiliary laser is tuned to the approximate center of gravity of the fine-structure transition in order to depopulate all the hyperfine levels of $5^2P_{3/2}$. A QWP removes any ellipticity in the beam and HWP sets the linear polarization orthogonal to that of the probe. The auxiliary beam is sent through the cell at a small angle relative to the pump beam. Inside the cell, the auxiliary beam is focused to a diameter $\phi_a \simeq 400$ µm, ensuring a complete spatial overlap with the probed area. The transmitted power of the auxiliary beam is detected by a Thorlabs PM100D power meter.

B. Evolution of the spin-noise variance and lineshape with the auxiliary beam power

Suppression of the quadratic spin-noise component. The impact of the excited-state depopulation due to the auxiliary beam is shown in Fig. 6. We fix all parameters as in Fig. 3: $P_p = 2\,\text{mW}$, $P_d = 0.4\,\text{mW}$, and $\Delta/2\pi = +1.5\,\text{GHz}$. The residuals of the spin-noise variance from the low-density linear fit are shown as a function of the vapor density for two cases: without the auxiliary beam (orange squares, same data as in Fig. 3) and with an 8 mW auxiliary beam (blue dots). Interestingly, in the latter case the residuals are zero up to a density of 3×10^{14} at. cm^{-3}, twice as much as compared with the "probe laser only" configuration. The spin-noise linearity is therefore partially retrieved: At the highest density, the nonlinear contribution is reduced by a factor of 3 by the auxiliary beam.

More insight on this noise reduction can be obtained by analyzing the impact of the auxiliary beam power, which governs the fraction of the initial excited-state population that is pumped away, at a fixed density of 3.3×10^{14} at. cm^{-3} ($T = 175\,^\circ$C). The results are shown in Fig. 6(b) (blue dots), along with the measured transmission of the auxiliary beam (orange triangles), which reflects changes in the population of the first excited state. When increasing the auxiliary beam power, the spin-noise residuals drop quickly, and the transmission of the auxiliary beam is simultaneously enhanced. This suggests that as the 776 nm beam depopulates the $5^2P_{3/2}$ state, the nonlinear scaling of the spin noise is suppressed. We fit the transmission data with a saturated transmission function $f(P_a) = L \exp\left(-\frac{\alpha_0}{1+P_a/P_s}\right)$, where α_0 is an unsaturated optical depth on the $5^2P_{3/2} \rightarrow 5^2D_{5/2}$ transition, P_s a saturation power, and L losses due to the cell windows. We find a typical saturation power of 1.7 mW. Consequently, for beam powers $P_a > 10\,\text{mW}$, the vapor is practically transparent to the 776 nm beam and the spin-noise residuals tend to zero. This again confirms that the linear scaling of spin noise with vapor density is restored when the excited-state population is quenched. On the contrary, we verified that at low density, i.e., in the noninteracting regime, the auxiliary beam power has no impact on the measured noise variance.

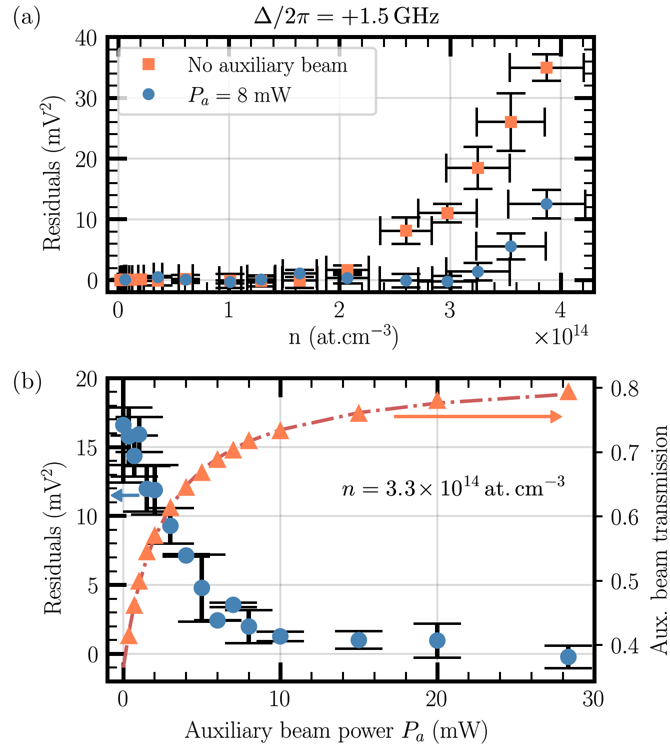

FIG. 6. Impact of the auxiliary beam on the detected spin-noise variance. (a) Density dependence of the residuals from the low-density linear trend with (blue dots) and without (orange squares) auxiliary beam. Parameters are $P_p = 2\,\text{mW}$, $P_d = 0.4\,\text{mW}$, and $\Delta/2\pi = +1.5\,\text{GHz}$. (b) Blue dots: Evolution of the residuals with auxiliary beam power at a fixed density of 3.3×10^{14} at. cm^{-3}. Orange triangles: Transmission of the auxiliary beam, fitted with a saturated optical depth function (red dash-dotted line).

Changes in lineshape. Finally, the spectral analysis of the detected signals allows us to correlate such results with a frequency redistribution of the spin noise. Figure 7(a) indeed shows a clear reshaping of the spin-noise spectra as the auxiliary beam power is increased from 0 to 28 mW. Specifically, one observes (1) *a narrowing* of the spin noise peaks and (2) *a reduction* of the broadband low-frequency noise, that is, a suppression of the hallmarks of the resonant dipole-dipole interaction [41].

This is confirmed by Fig. 7(b), which shows a reduction of the HWHM of the ^{85}Rb peak from almost 2 to 1 MHz (see blue dots). Such linewidths are obtained by locally fitting the SN peak centered on 10 MHz. This decay is well captured by a fitting function $f(P_a) = \gamma_0 + \frac{\delta\gamma}{1+P_a/P_s}$, where γ_0

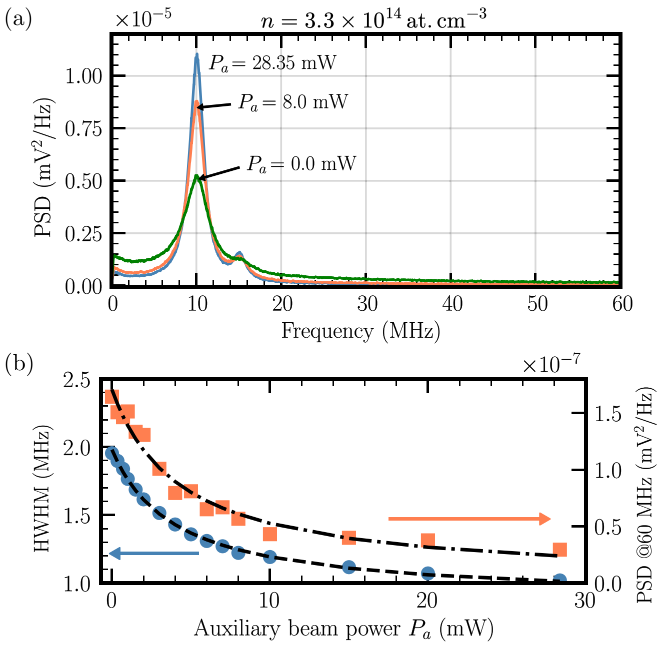

FIG. 7. Impact of the auxiliary beam power on the lineshapes. (a) Modification of the spin-noise line shapes with increasing auxiliary beam power depopulating the excited state. (b) Reduction of ^{85}Rb spin linewidth (blue dots) and broadband low-frequency noise measured at 60 MHz (orange squares). Dashed and dash-dotted line: fit by a saturation function.

is a supposedly unperturbed linewidth, $\delta\gamma$ is the interaction-induced broadening, and P_s is a saturation power of the excited-state transition in our experimental conditions. Such fitting function (in black dashed line) yields a saturation power of 4.0 ± 0.2 mW, larger but of the same order of magnitude as the one extracted from the transmission of the auxiliary beam. The unperturbed linewidth γ_0 is around 0.9 MHz, larger than the transit-limited 0.25 MHz linewidth, suggesting that a complete depletion of the excited states is not achieved due to the inhomogeneous Doppler broadening.

Additionally, a reduction of the broadband noise component centered on low frequencies is demonstrated by measuring the noise PSD level at a fixed frequency of 60 MHz, a region of the spectrum in which the SN peaks of both isotopes do not contribute. This noise level, shown in orange squares in Fig. 7(b), steadily decreases as the auxiliary beam power is increased. A similar fitting function as used for the linewidth yields a saturation power $P_s = 4.3 \pm 0.8$ mW in perfect agreement with the previous estimation. Eventually, the fact that both the spin-noise nonlinearity and lineshape distortions are suppressed by the auxiliary beam supports our claim that both features originate from dipole-dipole interactions in the vapor.

V. CONCLUSION

We have reported a previously unobserved nonlinear spin noise in a dense rubidium vapor, contrasting with the usual proportionality between spin variance and atomic density in dilute media. We have shown that a quadratic component in the spin variance appears for densities higher than 10^{14} at. cm^{-3}, together with strong distortions of the spin-noise spectrum attributed to light-induced dipole-dipole interaction in an earlier work. The impact of the optical excitation on the quadratic spin noise was confirmed by a strong dependence on the probe light power and detuning to atomic transitions between the $5^2S_{1/2}$ and $5^2P_{3/2}$ levels.

Based on our observations, we suggest that this anomalous scaling is due to positive atom-atom correlations arising due to resonant dipole-dipole interactions. Such interpretation is supported by a suppression of the nonlinear contribution to the total spin noise when inhibiting this interaction mechanism. This was achieved by tuning a second laser beam on the $5^2P_{3/2} \rightarrow 5^2D_{5/2}$ excited-state transition, thereby depopulating the first excited level. We experimentally demonstrated that a linear scaling of spin noise can be restored when saturating the absorption of the auxiliary beam, indicating an efficient reduction of atomic correlations.

These observations highlight the many-body nature of spin noise in physical systems where interactions allow interparticle correlations to build up. Moreover, our experimental observations suggest that the nonlinear spin–noise variance can be detected only beyond a critical threshold density, a feature often associated to phase transitions. Interestingly, Gorshkov *et al.* theoretically proved that spin-spin interactions could result in phase transitionlike changes in spin-noise dynamics [38], with an additional low-frequency noise component as a corresponding order parameter. Such predictions remarkably remind of the experimental results reported in Ref. [41] and in this article. Investigating any formal analogy between the two frameworks is thus an exciting perspective. In our case, which involves light-induced processes rather than direct spin interactions, the role of multiple photon scattering at unit optical depths should also be clarified.

Another natural and interesting follow-up prospect is the clarification of the quantum or classical statistics of such correlations. This is usually done by comparing spin variance with relevant lower-bound inequalities [50], with the additional difficulty of having here positive correlations rather than the negative ones usually associated to spin squeezing [51]. Whether spin fluctuations are Gaussian or not in the correlated regime is an important related question, and could in principle be investigated using higher-order SNS [52–54]. Solving these questions could improve our knowledge of collective effects in dense atomic vapors and spin dynamics in open, many-body-correlated ensembles.

ACKNOWLEDGMENTS

The authors thank Antoine Browaeys and Thomas F. Cutler for their help with the vapor cell, Ehouarn Le Roy and Jiong Deng for their experimental support, and from Sébastien Rousselot for technical assistance. This work benefited from useful discussions with Kostas Mouloudakis and Jan Kołodyński. The authors warmly thank Iannis Kominis for his insight and suggestions regarding the protocol described in Sec. IV. The authors acknowledge funding by the Labex PALM.

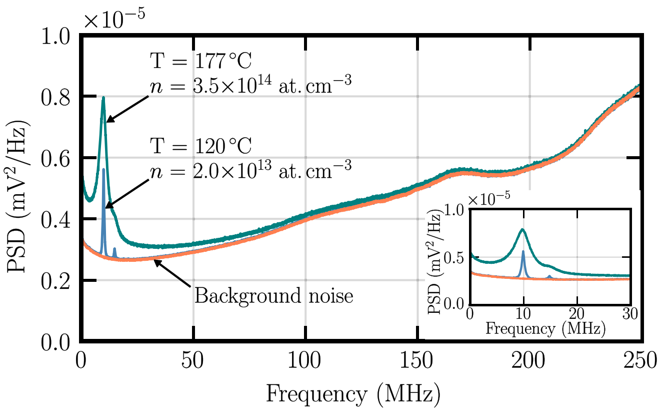

FIG. 8. Examples of raw PSD along with total background noise. Integration bounds for spin-noise variance calculations are determined by the frequencies around which the total PSD merges with the background.

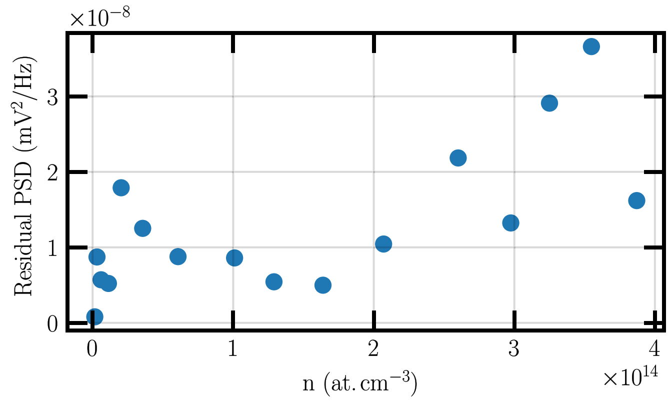

FIG. 9. Examples of residual PSD levels after background subtraction, from which uncertainties in the estimated spin-noise variance are derived.

DATA AVAILABILITY

There are no publicly available research data or software supporting this manuscript. Requests for further information or data should be sent to the authors.

APPENDIX A: BACKGROUND SUBTRACTION AND INTEGRATION PROCEDURE

1. Background subtraction

We describe here the procedure for extracting and analyzing the spin-noise signal obtained from the digital oscilloscope. In order to properly evaluate the integral of the spin-noise PSD, accurate subtraction of the background is imperative. In our experiment, the background is composed of two contributions: (1) the dark background of the balanced photodetector, amplification chain, and oscilloscope, and (2) the laser shot noise. We systematically subtract these two backgrounds using the following procedure:

(1) We first acquire the dark electronic background noise $S_{\text{elec}}(\nu)$, with the laser turned off. This includes the technical background noise of the whole detection chain.

(2) We then acquire the background S_{bg} with the laser on but no vapor cell. This contains both the laser shot noise $S_{\text{laser}}(\nu)$ and the dark electronic background $S_{\text{bg}}(\nu) = S_{\text{elec}}(\nu) + S_{\text{laser}}(\nu)$. The laser shot noise can be thus accessed by performing the subtraction $S_{\text{laser}} = S_{\text{bg}} - S_{\text{elec}}$. The orange curve labeled "background noise" in Fig. 8 shows a typical background signal extending across the full range of measured frequencies.

Subsequently, the total measured signal, S_{meas}, is a combination of the electronic background, the laser shot noise and the actual atomic response itself. Two such curves measured at 120 °C and 177 °C are shown in Fig. 8. Note that the background noise steadily increasing after 200 MHz is mainly due to the oscilloscope electronic noise and is thus not limited by the photodetection bandwidth (the frequency response of the whole detection scheme is shown in Appendix B). To prevent aliasing (spectral folding) due to the 1 GHz sampling rate (500 MHz Nyquist frequency), we purposefully reduce the oscilloscope analog bandwidth to 350 MHz, below the maximum 500 MHz bandwidth. The inset figure shows a close-up view up to 30 MHz, highlighting the main spin-noise peaks. The spin-noise signal S_{SN} is retrieved from the measured signal by subtracting the total background, i.e., $S_{\text{SN}} = S_{\text{meas}} - S_{\text{bg}}$. Residual background levels remaining after this experimental baseline subtraction are determined and eliminated as described in the following subsection. The final form of the PSD is shown in other parts of the text [Figs. 2 and 7(a)].

2. PSD integration procedure

In order to obtain the spin-noise variance, S_{SN} is then integrated by manually choosing an appropriate frequency domain. The total spin-noise variance is composed of contributions from the resonance peaks of ^{85}Rb and ^{87}Rb as well as the broadband noise component appearing at higher densities. Hence, the integration frequency range should appropriately account for all these contributions.

At high densities, the broadening of the peaks and the additional broadband noise component implies the need for a large integration domain (see green curve in Fig. 8). On the lower end, the minimal bound is always limited by the 0.2 MHz cutoff frequency from the high-pass filtering. The upper bound is chosen where S_{SN} significantly merges with S_{bg} for each spectrum, within a limit of around 250 MHz (see next Appendix A 3). For spectra taken at lower density, the only relevant contribution to the spin-noise signal comes from the two narrow SN peaks. This can be seen in Fig. 8, where, apart from the two sharp resonance features, the signal for $n = 2.0 \times 10^{14}$ at. cm^{-3} ($T = 120\,^\circ$C) is flat and overlaps with the background S_{bg}. Hence, the integration domain is chosen in the near vicinity of these peaks, typically between 7 and 20 MHz, to avoid systematic errors in the estimation of the spin variance, as discussed below.

After having fixed the integration bounds, we further quantify any potential residual background by averaging the PSD S_{SN} in a 10 MHz range around the chosen higher cutoff frequency. An example of the obtained residual PSD is shown in Fig. 9 for $\Delta/2\pi = +1.5$ GHz and a detection power of 400 µW. These remaining PSD levels are then considered as an imperfect background calibration, are subtracted from the

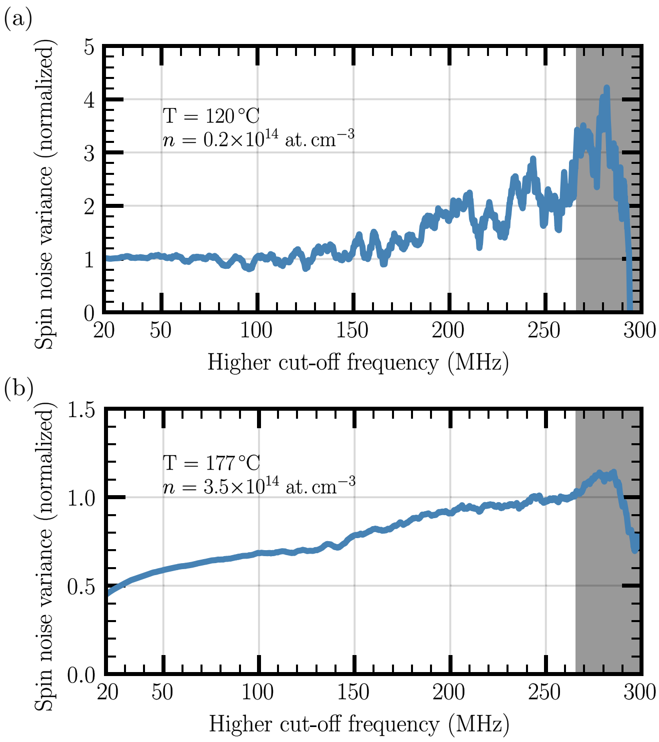

FIG. 10. Impact of the upper integration frequency bound on the estimated spin-noise variance at (a) $n = 2 \times 10^{13}$ at. cm^{-3} and (b) $n = 3.5 \times 10^{14}$ at. cm^{-3}. The shaded gray area marks a region where technical electronic noises systematically remain after our background subtraction procedure.

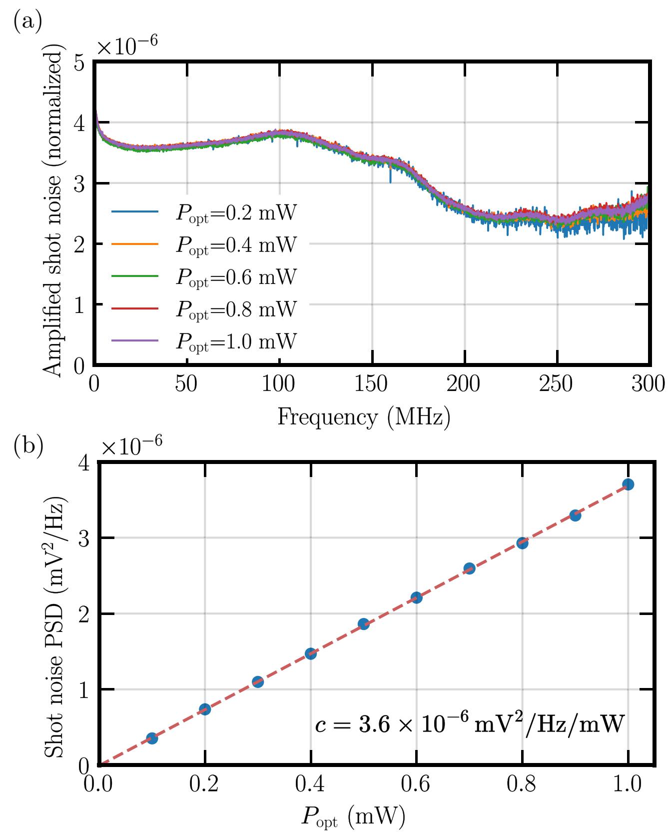

FIG. 11. Characterization of the photon shot noise power spectrum. (a) PSD of the detected shot noise for different optical powers, after normalization by this power. (b) Linearity of the shot noise PSD evaluated at a fixed 10 MHz frequency with input optical power.

corresponding data, and are used to derive the error bars in the spin-noise variance plots in the main text.

3. Impact of the integration bandwidth

We discuss here the sensitivity of the measured spin-noise variance on the choice of the upper integration cutoff frequency. We show in Fig. 10 the integrated spin-noise variance for $\Delta/2\pi = +1.5\,\text{GHz}$, $P_d = 400\,\mu\text{W}$, as a function of the higher frequency bound for a low density ($n = 2 \times 10^{13}$ at. cm^{-3}) and a high density ($n = 3.5 \times 10^{14}$ at. cm^{-3} spectrum). The values are normalized by the final estimated variance displayed in Fig. 4.

At low density, one clearly sees in Fig. 10(a) that the estimated integrated variance does not depend on the upper bound if it is chosen in the vicinity of the ^{87}Rb peak (centered on 15 MHz). As soon as it gets larger than 50 MHz, fluctuations in the estimated value appear, eventually leading to errors of more than 50% above 150 MHz. This is due to the weak signal-to-noise ratio and imperfect experimental background subtraction, which leads to the unnecessary integration of baseline fluctuations in parts of the spectrum that do not contain spin-noise information. We thus restrict the integration range as close to the spin-noise resonances as possible, as explained in the previous section.

For high-density spectra, the role of the higher cutoff frequency is more critical. Since the signal is stronger, no fluctuations due to the background subtraction are visible as in the low-density case. However, because of the very broad low-frequency noise, the integrated spin-noise variance increases steadily up to frequencies as high as 250 MHz. Above 270 MHz (gray shaded area in Fig. 10), the noise is dominated by an uncompensated oscilloscope electronic background noise. This forces us to set a limit around 250 MHz on the upper frequency range. Finally, note that our conclusions regarding the nonlinear density dependence are robust against this choice of integration range: For $n = 3.5 \times 10^{14}$ at. cm^{-3}, the experimental spin-noise level already exceeds the prediction of the low-density linear regression and the light-atom coupling model ($\simeq 50\,\text{mV}^2$) for an upper integration range as low as 70 MHz, which is clearly insufficient as seen in Fig. 10(b).

APPENDIX B: LINEARITY OF THE PHOTODETECTION

We experimentally show here that the observed nonlinearities and lineshape changes at higher densities are not an artifact of the photodetector and that all the measurements are performed within the linear regime of the detector.

We measure the laser shot-noise signal at different optical powers, while balancing the detection for each measurement, by getting rid of the vapor cell on the beam path. Figure 11(a) shows the detected shot noise PSD $S_{\text{laser}}(\nu)$ after subtraction of the electronic background (see Appendix A), at five different optical powers P_{opt} ranging from 0.2 to 1.0 mW. Our usual detection power of 0.4 mW lies well within this range. Since we expect a shot noise power $S_{\text{laser}} \propto P_{\text{opt}}$, each curve is normalized by dividing the corresponding optical power. It is clear that the scaled PSDs at all measured optical powers fall on top of each other, indicating a good linearity of our photodection scheme over a 300 MHz frequency range. Note that since photon shot noise is a white noise, Fig. 11(a) also gives away the frequency response function of the detection and amplification chain, which is used to normalize the computed spin-noise spectra.

Furthermore, Fig. 11(b) shows the shot-noise level measured at 10 MHz as a function of the optical power. This frequency is chosen to show the linearity of the PSD near the resonance peaks within the area of interest. A linear fit gives a slope of $s_{\text{exp}} = 3.6 \times 10^{-6}\ \text{mV}^2/(\text{Hz mW})$. The theoretically expected slope calculated using the datasheet of Thorlabs PDB435A at a transimpedance gain of 10^4 V/A and a responsivity of 0.47 A/W at 780 nm is precisely $3.6 \times 10^{-6}\ \text{mV}^2/(\text{Hz mW})$, in excellent agreement with the experimental data.

APPENDIX C: CALCULATIONS OF ABSOLUTE FARADAY ROTATION NOISE VARIANCE

We consider an ensemble of atoms having a simple electronic spin degree of freedom in the ground state. Let us assume that this ensemble has a finite average magnetization in the z direction, denoted $\langle S_z\rangle = \frac{1}{N}\sum_k \langle s_z^{(k)}\rangle$, where N is the number of probed atoms and $s_z^{(k)}$ the single-particle spin operator of atom k. A linearly polarized probe beam propagating along z in the vapor while being tuned near an atomic resonance will experience a polarization rotation by an angle φ due to the Faraday effect. Denoting d_0 the dipole matrix element of the nearby transition, Δ the detuning, k the light wave vector, and L the cell length, it is given by

$$\varphi = \frac{d_0^2 knL}{6\varepsilon_0\hbar\Delta}\langle S_z\rangle\,. \tag{C1}$$

This result can be obtained by following the derivations of Refs. [43] or [12], which are formulated in terms of oscillator strength of the atomic transition rather than reduced dipole elements as we choose here. Note that this equation is valid in the limit $\Delta \gg \Gamma_0, \Gamma_D$, where Γ_0 denotes the excited-state population decay rate and Γ_D the Doppler inhomogeneous broadening. In Sec. II B, for instance, we typically have a detuning $\Delta \simeq 5 \times \Gamma_D$ to the closest hyperfine transitions of ^{85}Rb; hence, we are not strictly in the limit $\Delta \gg \Gamma_D$. We still chose to overlook the Doppler broadening and use Eq. (C1) here, since these calculations only aim at providing an estimation of the spin-noise level to validate our experimental protocol.

In our case, the cell contains two isotopes [labeled by the superscript (i)], showing spin-orbit and hyperfine coupling due to their nuclear magnetic moment $I^{(i)}$. One must now use the projection theorem to express the electronic spin operator as a function of the set of hyperfine spin operator F_z, and take into account the detuning Δ_F to each transition between a ground-state hyperfine F level and the excited state. Here, we neglect the excited-state hyperfine splitting, which is unresolved due to Doppler broadening in warm rubidium vapors. The Faraday rotation angle then writes

$$\varphi = \frac{d_0^2 knL}{6\varepsilon_0\hbar}\sum_i\sum_F \varepsilon_F \frac{A_i}{2I^{(i)}+1}\frac{\langle F_z^{(i)}\rangle}{\Delta_F}, \tag{C2}$$

where n is the total atom density, A_i is the abundance of isotope i, and $\varepsilon_F = \pm 1$ for $F = I^{(i)} \pm 1/2$, respectively. We use the definition of d_0 given by $\Gamma_0 = \frac{d_0^2\omega_0^3}{3\hbar\varepsilon_0 c^3}\frac{2J+1}{2J'+1}$, with c the speed of light in vacuum, and ω_0 the transition frequency between ground and excited states with respective electronic angular momentum J and J'. For the D_2 transition of rubidium, $d_0 = 3.58 \times 10^{-29}$ C m [42].

In SNS experiments, the vapor is unpolarized, so that $\langle F_z^{(i)}\rangle = 0$ for every i and F. We measure the variance of the Faraday angle $\langle\varphi^2\rangle$,

$$\langle\varphi^2\rangle = \left[\frac{d_0^2 knL}{6\varepsilon_0\hbar}\right]^2 \sum_i\sum_F \frac{A_i^2}{[2I^{(i)}+1]^2}\frac{\left\langle\left(F_z^{(i)}\right)^2\right\rangle}{\Delta_F^2}. \tag{C3}$$

The variance of the z component of all hyperfine spin operators writes [27,35]

$$\left\langle\left(F_z^{(i)}\right)^2\right\rangle = \frac{1}{N_i}\frac{F(F+1)(2F+1)}{6(2I^{(i)}+1)} = \frac{\langle f_z^2\rangle}{N_i}, \tag{C4}$$

where f_z is a single-atom hyperfine spin operator. We used here the assumption of a mixed state $\rho_N = \rho_{\text{th}}^{\otimes N}$, with ρ_{th} the single-atom thermal state, to describe a noninteracting ensemble of atoms at high temperature. Note that we already neglected correlations between different hyperfine levels in Eq. (C3), in agreement with the hypothesis of an uncorrelated ensemble.

The total number of probed atoms being $N = nL\Sigma$, where Σ denotes the effective probe beam area, and the total Faraday rotation noise variance finally writes

$$\langle\varphi^2\rangle = \alpha^2\frac{nL}{\Sigma}\sum_i\sum_F \frac{A_i}{[2I^{(i)}+1]^2}\frac{\left\langle\left(f_z^{(i)}\right)^2\right\rangle}{\Delta_F^2}, \tag{C5}$$

where $\alpha = \frac{d_0^2 k}{6\varepsilon_0\hbar}$ is an optical coupling factor reminiscent of the atomic polarizability.

Let us emphasize here that the proportionality of $\langle\varphi^2\rangle$ with the atom density n directly originate from the approximation of uncorrelated atoms. It is this approximation that we believe breaks down at higher density and could explain the results reported in this article.

Finally, taking into account the optically detected power P_d, the balanced detection sensitivity η, transimpedance R_t, and an additional amplification gain $g_{\text{dB}} = 23.8$ dB, the experimentally measured voltage variance is

$$\langle V^2\rangle = \left[2\eta R_t P_d \times 10^{\frac{g_{\text{dB}}}{20}}\right]^2\langle\varphi^2\rangle\,. \tag{C6}$$

These equations are used with the relevant beam size parameters and electronic specifications to calculate the theoretical voltage variance in the experiment presented in Sec. II B.

[1] A. L. Bloom, Principles of operation of the rubidium vapor magnetometer, Appl. Opt. **1**, 61 (1962).
[2] D. Budker and M. Romalis, Optical magnetometry, Nat. Phys. **3**, 227 (2007).
[3] B. L. Schmittberger and D. R. Scherer, A review of contemporary atomic frequency standards, arXiv:2004.09987.
[4] A. Bauch, Caesium atomic clocks: Function, performance and applications, Meas. Sci. Technol. **14**, 1159 (2003).
[5] I. Novikova, A. V. Gorshkov, D. F. Phillips, A. S. Sørensen, M. D. Lukin, and R. L. Walsworth, Optimal control of light pulse storage and retrieval, Phys. Rev. Lett. **98**, 243602 (2007).
[6] W. Tittel, M. Afzelius, T. Chanelière, R. L. Cone, S. Kröll, S. A. Moiseev, and M. Sellars, Photon-echo quantum memory in solid state systems, Laser Photon. Rev. **4**, 244 (2010).
[7] N. Sangouard, C. Simon, Hugues de Riedmatten, and Nicolas Gisin, quantum repeaters based on atomic ensembles and linear optics, Rev. Mod. Phys. **83**, 33 (2011).
[8] I. H. Deutsch, Harnessing the power of the second quantum revolution, PRX Quantum **1**, 020101 (2020).
[9] V. Scarani, H. Bechmann-Pasquinucci, N. J. Cerf, M. Dušek, N. Lütkenhaus, and M. Peev, The security of practical quantum key distribution, Rev. Mod. Phys. **81**, 1301 (2009).
[10] F. Xu, X. Ma, Q. Zhang, H.-K. Lo, and J.-W. Pan, Secure quantum key distribution with realistic devices, Rev. Mod. Phys. **92**, 025002 (2020).
[11] E. B. Aleksandrov and V. S. Zapasskii, Magnetic resonance in the Faraday-rotation noise spectrum, Zh. Eksp. Teor. Fiz. **81**, 132 (1981) [Sov. Phys. JET **54**, 64 (1981)].
[12] S. A. Crooker, D. G. Rickel, A. V. Balatsky, and D. L. Smith, Spectroscopy of spontaneous spin noise as a probe of spin dynamics and magnetic resonance, Nature (London) **431**, 49 (2004).
[13] B. Mihaila, S. A. Crooker, D. G. Rickel, K. B. Blagoev, P. B. Littlewood, and D. L. Smith, Quantitative study of spin noise spectroscopy in a classical gas of ^{41}K atoms, Phys. Rev. A **74**, 043819 (2006).
[14] G. E. Katsoprinakis, A. T. Dellis, and I. K. Kominis, Measurement of transverse spin-relaxation rates in a rubidium vapor by use of spin-noise spectroscopy, Phys. Rev. A **75**, 042502 (2007).
[15] S. Liu, P. Neveu, J. Delpy, L. Hemmen, E. Brion, E. Wu, F. Bretenaker, and F. Goldfarb, Birefringence and dichroism effects in the spin noise spectra of a spin-1 system, New J. Phys. **24**, 113047 (2022).
[16] M. Oestreich, M. Römer, R. J. Haug, and D. Hägele, Spin noise spectroscopy in GaAs, Phys. Rev. Lett. **95**, 216603 (2005).
[17] J. Hübner, F. Berski, R. Dahbashi, and M. Oestreich, The rise of spin noise spectroscopy in semiconductors: From acoustic to GHz frequencies, Physica Status Solidi (b) **251**, 1824 (2014).
[18] S. V. Poltavtsev, I. I. Ryzhov, M. M. Glazov, G. G. Kozlov, V. S. Zapasskii, A. V. Kavokin, P. G. Lagoudakis, D. S. Smirnov, and E. L. Ivchenko, Spin noise spectroscopy of a single quantum well microcavity, Phys. Rev. B **89**, 081304(R) (2014).
[19] P. Glasenapp, D. S. Smirnov, A. Greilich, J. Hackmann, M. M. Glazov, F. B. Anders, and M. Bayer, Spin noise of electrons and holes in (In, Ga)As quantum dots: Experiment and theory, Phys. Rev. B **93**, 205429 (2016).
[20] V. O. Kozlov, N. S. Kuznetsov, A. N. Kamenskii, A. Greilich, I. I. Ryzhov, G. G. Kozlov, and V. S. Zapasskii, Spin noise of magnetically anisotropic centers, Phys. Rev. B **107**, 064427 (2023).
[21] V. O. Kozlov, I. A. Smirnov, M. S. Kuznetsova, E. V. Kolobkova, G. G. Kozlov, V. S. Zapasskii, D. S. Smirnov, and I. I. Ryzhov, Spin noise reveals spin dynamics and recharging of lead halide perovskite nanocrystals, Appl. Mater. Today **45**, 102820 (2025).
[22] P. Glasenapp, N. A. Sinitsyn, L. Yang, D. G. Rickel, D. Roy, A. Greilich, M. Bayer, and S. A. Crooker, Spin noise spectroscopy beyond thermal equilibrium and linear response, Phys. Rev. Lett. **113**, 156601 (2014).
[23] M. Swar, D. Roy, D. Dhanalakshmi, S. Chaudhuri, S. Roy, and H. Ramachandran, Measurements of spin properties of atomic systems in and out of equilibrium via noise spectroscopy, Opt. Express **26**, 32168 (2018).
[24] T.-J. Sun, P. Sterin, L. Lengert, C. Nawrath, M. Jetter, P. Michler, Y. Ji, J. Hübner, and M. Oestreich, Non-equilibrium spin noise spectroscopy of a single quantum dot operating at fiber telecommunication wavelengths, J. Appl. Phys. **131**, 065703 (2022).
[25] J. Delpy, S. Liu, P. Neveu, E. Wu, F. Bretenaker, and F. Goldfarb, Spin-noise spectroscopy of optical light shifts, Phys. Rev. A **107**, L011701 (2023).
[26] T. Sato, S. Watanabe, M. Matsuo, and T. Kato, Fluctuations in spin dynamics excited by pulsed light, Phys. Rev. Lett. **134**, 106702 (2025).
[27] V. Shah, G. Vasilakis, and M. V. Romalis, High bandwidth atomic magnetometery with continuous quantum nondemolition measurements, Phys. Rev. Lett. **104**, 013601 (2010).
[28] K. Mouloudakis, V. Koutrouli, I. K. Kominis, M. W. Mitchell, and G. Vasilakis, Spin projection noise and the magnetic sensitivity of optically pumped magnetometers, arXiv:2402.10746.
[29] Y. Li, X. Li, T. Guo, and K. Zhao, Spin dynamics and noise spectrum for alkali-metal atoms of arbitrary polarization in the spin-exchange-relaxation-free regime, Phys. Rev. A **111**, 033703 (2025).
[30] V. G. Lucivero, R. Jiménez-Martínez, J. Kong, and M. W. Mitchell, Squeezed-light spin noise spectroscopy, Phys. Rev. A **93**, 053802 (2016).
[31] C. Troullinou, R. Jiménez-Martínez, J. Kong, V. G. Lucivero, and M. W. Mitchell, Squeezed-light enhancement and backaction evasion in a high sensitivity optically pumped magnetometer, Phys. Rev. Lett. **127**, 193601 (2021).
[32] V. Guarrera, R. Gartman, G. Bevilacqua, and W. Chalupczak, Spin-noise spectroscopy of a noise-squeezed atomic state, Phys. Rev. Res. **3**, L032015 (2021).
[33] J. Meineke, J.-P. Brantut, D. Stadler, T. Müller, H. Moritz, and T. Esslinger, Interferometric measurement of local spin fluctuations in a quantum gas, Nat. Phys. **8**, 454 (2012).
[34] M. Swar, D. Roy, S. Bhar, S. Roy, and S. Chaudhuri, Detection of spin coherence in cold atoms via Faraday rotation fluctuations, Phys. Rev. Res. **3**, 043171 (2021).
[35] K. Mouloudakis, G. Vasilakis, V. G. Lucivero, J. Kong, I. K. Kominis, and M. W. Mitchell, Effects of spin-exchange collisions on the fluctuation spectra of hot alkali-metal vapors, Phys. Rev. A **106**, 023112 (2022).
[36] K. Mouloudakis, F. Vouzinas, A. Margaritakis, A. Koutsimpela, G. Mouloudakis, V. Koutrouli, M. Skotiniotis, G. P. Tsironis, M. Loulakis, M. W. Mitchell, G. Vasilakis, and I. K. Kominis, Interspecies spin-noise correlations in hot atomic vapors, Phys. Rev. A **108**, 052822 (2023).

[37] D. Roy, L. Yang, S. A. Crooker, and N. A. Sinitsyn, Cross-correlation spin noise spectroscopy of heterogeneous interacting spin systems, Sci. Rep. **5**, 9573 (2015).

[38] V. N. Gorshkov, M. O. Stretovych, N. A. Sinitsyn, and D. Mozyrsky, Phase transition in the noise power spectrum of interacting-spin fluctuations at infinite temperature, Phys. Rev. B **109**, 094402 (2024).

[39] J. Schlegel, M. Evers, and U. Nowak, Spin-noise spectroscopy as a tool for probing magnetic order, arXiv:2411.18342.

[40] D. Roy, R. Singh, and R. Moessner, Probing many-body localization by spin noise spectroscopy, Phys. Rev. B **92**, 180205(R) (2015).

[41] J. Delpy, N. Fayard, F. Bretenaker, and F. Goldfarb, Anomalous high-density spin noise in a strongly interacting atomic vapor, Phys. Rev. Res. **7**, 013298 (2025).

[42] D. A. Steck, Rubidium 85 D line data, 2001, https://steck.us/alkalidata/.

[43] G. Vasilakis, Precision measurements of spin interactions with high density atomic vapors, Ph.D. thesis, Princeton University, 2011.

[44] M. Koschorreck, M. Napolitano, B. Dubost, and M. W. Mitchell, Quantum nondemolition measurement of large-spin ensembles by dynamical decoupling, Phys. Rev. Lett. **105**, 093602 (2010).

[45] M. Koschorreck, M. Napolitano, B. Dubost, and M. W. Mitchell, Sub-projection-noise sensitivity in broadband atomic magnetometry, Phys. Rev. Lett. **104**, 093602 (2010).

[46] K. Shibata, N. Sekiguchi, J. Takai, and T. Hirano, Dispersive measurement of spin shot noise in a Bose-Einstein condensate, Phys. Rev. Res. **7**, 043040 (2025).

[47] W. Happer and B. S. Mathur, Effective operator formalism in optical pumping, Phys. Rev. **163**, 12 (1967).

[48] W. Happer, Light propagation and light shifts in optical pumping experiments, Prog. Quantum Electron. **1**, 51 (1970).

[49] G. Grynberg, A. Aspect, and C. Fabre, *Introduction to Quantum Optics: From the Semi-Classical Approach to Quantized Light* (Cambridge University Press, 2010).

[50] G. Vitagliano, I. Apellaniz, I. L. Egusquiza, and G. Tóth, Spin squeezing and entanglement for an arbitrary spin, Phys. Rev. A **89**, 032307 (2014).

[51] J. Kong, R. Jiménez-Martínez, C. Troullinou, V. G. Lucivero, G. Tóth, and M. W. Mitchell, Measurement-induced, spatially-extended entanglement in a hot, strongly-interacting atomic system, Nat. Commun. **11**, 2415 (2020).

[52] N. A. Sinitsyn and Y. V. Pershin, The theory of spin noise spectroscopy: A review, Rep. Prog. Phys. **79**, 106501 (2016).

[53] F. Li, A. Saxena, D. Smith, and N. A Sinitsyn, Higher-order spin noise statistics, New J. Phys. **15**, 113038 (2013).

[54] F. Li and N. A. Sinitsyn, Universality in higher order spin noise spectroscopy, Phys. Rev. Lett. **116**, 026601 (2016).